GEOPHYSICS, VOL. 67, NO. 3 (MAY-JUNE 2002); P. 701–710, 14 FIGS.
10.1190/1.1484513

Multicomponent AVO analysis, Vacuum field, New Mexico

Bryan DeVault*, Thomas L. Davis‡, Ilya Tsvankin**, Richard Verm§, and Fred Hilterman§

ABSTRACT

Shear-wave amplitude variation with offset (AVO) analysis can be used to map changes in density, shear-wave velocity, and fracturing at reservoir scale by allowing the influence of each factor to be separately extracted from the observed seismic response. Weighted least-squares inversion of the anisotropic reflection coefficients was implemented to find the shear-wave splitting coefficient and velocity-contrast parameters. A time-lapse nine-component, 4-D seismic survey acquired over Vacuum field in Lea County, New Mexico, was used to test our methodology of shear-wave AVO analysis and to compare the results with well production and azimuthal *P*-wave AVO analysis.

Weighted least-squares shear-wave AVO stacks of the splitting parameter were found to be excellent predictors of well fluid-production performance, implying a strong link between seismically inferred fracturing and reservoir-scale permeability of the San Andres dolomites at Vacuum field. Analysis of the shear-wave velocity contrast indicated the presence of a second set of open fractures to the south of a carbon dioxide injector well where a 4-D anomaly associated with injection had been observed.

INTRODUCTION

The Reservoir Characterization Project at the Colorado School of Mines acquired two 3-D, nine-component (9-C) seismic surveys during the fall of 1995 to monitor possible changes in observed seismic signatures caused by a pilot carbon dioxide huff and puff injection project at a single borehole, CVU-95 (Roche et al., 1997). Vacuum field is located on the Northwest Shelf of the Central Basin Platform in Lea County, New Mexico, approximately 25 miles (40 km) west–southwest of Hobbs (Figure 1). It produces from several Permian-age formations, most notably the Guadalupian San Andres, which has yielded almost 230 million barrels of oil since its discovery in 1929 (Bebout and Harris, 1990). The stratigraphic section in the Vacuum field area is dominated by dolomitized platform/shelf carbonates. A stratigraphic column for the Vacuum field area is shown in Figure 2. The Upper San Andres, the main focus of this study, is a heterogeneous dolomite which varies in thickness over the study area from approximately 150 ft (46 m) to more than 230 ft (70 m) (Scuta, 1997). Average porosity in the San Andres varies between approximately 6% and 12%. Structural dips over the field at the San Andres level are slight, averaging less than 3°—a fact which considerably simplifies AVO analysis.

A baseline 3-D, 9-C seismic survey (Figure 3) was acquired in October 1995 using east–west source lines spaced 605 ft (184 m) apart and orthogonal north–south receiver lines with a 495-ft (151-m) line spacing (Roche, 1997). Both source and receiver station intervals were 110 ft (33 m), giving a natural survey bin size of 55 ft (17 m). Point arrays of three-component geophones were deployed at each station, and both *P*- and shear-wave vibrators were used for acquisition. A monitor seismic survey using the same parameters and the same source and receiver locations followed in December 1995. The resulting seismic data sets were well suited for AVO analysis because they were richly sampled in both offset and azimuth, providing an ample number of both offset and azimuth data sets.

Fracturing at the San Andres level in Vacuum field, though not intense, is observed in cores and is thought to be the cause of shear-wave splitting detected over the reservoir on VSPs and surface seismic data (Voorhies, 1996). Well production is influenced by the presence of these fractures, which are dominantly open in the direction of modern-day maximum compressive horizontal stress (Scuta, 1997). No simple relation between average porosity and well productivity is apparent, strengthening the conclusion that fractures play an important role in well

Presented at the 68th Annual Meeting, Society of Exploration Geophysicists. Manuscript received by the Editor March 6, 2000; revised manuscript received September 21, 2001.
*Formerly Colorado School of Mines, Golden, Colorado; presently Anadarko Petroleum Corporation, 1201 Lake Robbins Dr., The Woodlands, Texas 77380. E-mail: b_devault@yahoo.com.
‡Colorado School of Mines, Department of Geophysics, Golden, Colorado 80401. E-mail: tdavis@mines.edu.
**Colorado School of Mines, Center for Wave Phenomena, Department of Geophysics, Golden, Colorado 80401.
§Geophysical Development Corporation, One Riverway, Suite 2100, Houston, Texas 77056. E-mail: fred@geodev.com.

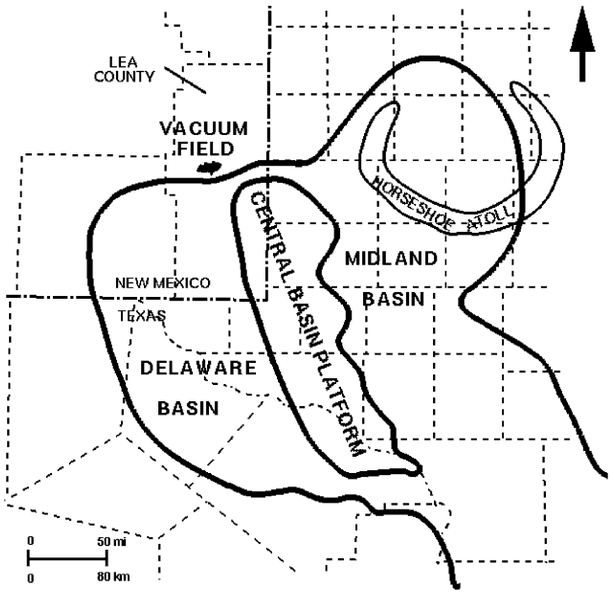

FIG. 1. Location map of Vacuum field, After Blaylock (1999).

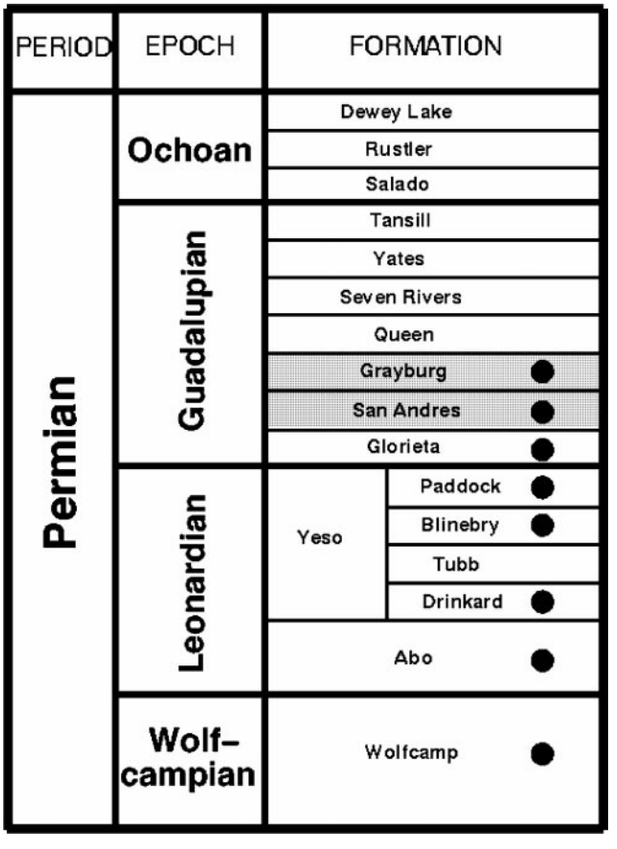

FIG. 2. Generalized stratigraphic column, showing Permian section present in Vacuum field area. Productive intervals are indicated, with Grayburg and San Andres Formations shaded. After Blaylock (1999).

behavior. The principal objective of the multicomponent AVO analysis techniques developed and applied to the Vacuum field seismic data sets was mapping lateral changes in the intensity of these fractures and correlating the amount of fracturing with well production.

THEORY OF MULTICOMPONENT AVO ANALYSIS

The purpose of amplitude variation with offset (AVO) analysis is to infer information about lithology, pore fill, or fracturing from prestack reflection seismic data. As with all other geophysical techniques, a theoretical model is required to interpret observed AVO behavior, and AVO results are relative observations of lateral changes rather than absolute measurements. The simplest azimuthally anisotropic AVO model, which can be conveniently used for constructing small-contrast plane-wave reflection coefficients linearized in density, velocity, and anisotropy parameters, is that of horizontal transverse isotropy (HTI). This model results from assuming an isotropic matrix containing a set of vertical, aligned, penny-shaped inclusions (fractures); it has a horizontal symmetry axis and two vertical symmetry planes. One is defined by the symmetry-axis plane that contains the symmetry axis, while the perpendicular isotropy plane is parallel to the fracture faces (Rueger, 1996). Waves confined to the isotropy plane do not experience any velocity variation with angle, because the model is rotationally invariant with respect to the symmetry axis. Polarizations of vertically traveling shear waves in HTI media are confined to the symmetry-axis plane (the slow, or S_2 mode) and to the isotropy plane (the fast, or S_1 mode), with the splitting parameter γ approximately equal to the fractional difference between the velocities of the two modes.

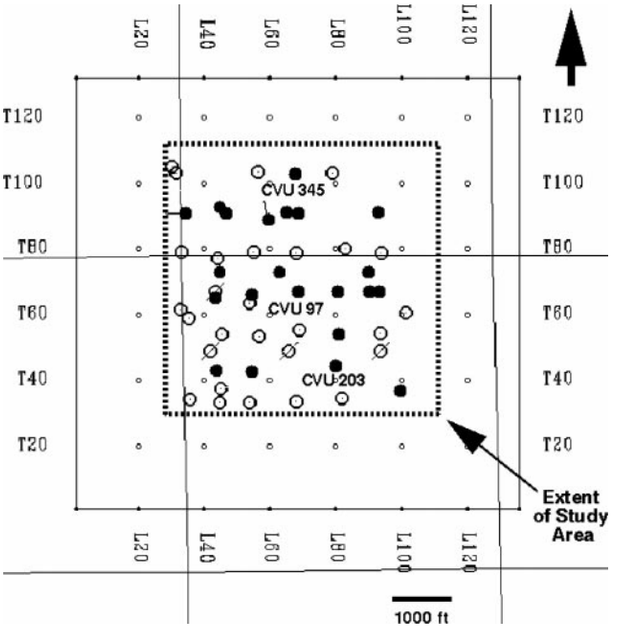

FIG. 3. Central Vacuum field base map showing wells used for study, approximate study area outline, and seismic survey in-lines (designated L) and cross-lines (designated T). The carbon dioxide injector well CVU-97 is shown at the center of the survey. After Blaylock (1999).

Tsvankin (1997) and Rueger (1996) derived an elegant parameterization for HTI symmetry in terms of Thomsen-style parameters δ^v, ε^v, and γ[δ^v is defined in terms of the elastic moduli as $((c_{13}+c_{55})^2-(c_{33}-c_{55})^2)/(2c_{33}(c_{33}-c_{55}))$, while ε^v is defined as $(c_{11}-c_{33})/2c_{33}$]. Using this parameterization, the linearized, small-contrast approximation for the plane-wave reflection coefficient can be written in matrix form as a function of incident phase angle θ as (Rueger, 1998)

$$R_2^{str}(\theta) = -\frac{1}{2}\left(\frac{\Delta\beta}{\beta}+\frac{\Delta\rho}{\rho}-\Delta\gamma\right)+\frac{1}{2}\left(\frac{\Delta\beta}{\beta}-\Delta\gamma\right)\tan^2\theta,$$

$$R_1^{str}(\theta) = -\frac{1}{2}\left(\frac{\Delta\beta}{\beta}+\frac{\Delta\rho}{\rho}\right)+\left(\frac{7}{2}\frac{\Delta\beta}{\beta}+2\frac{\Delta\rho}{\rho}\right)\sin^2\theta,$$

$$R_1^{sym}(\theta) = -\frac{1}{2}\left(\frac{\Delta\beta}{\beta}+\frac{\Delta\rho}{\rho}\right)+\frac{1}{2}\left(\frac{\Delta\beta}{\beta}-\Delta\gamma\right)\tan^2\theta,$$

$$R_2^{sym}(\theta) = -\frac{1}{2}\left(\frac{\Delta\beta}{\beta}+\frac{\Delta\rho}{\rho}-\Delta\gamma\right)+\left[\frac{7}{2}\left(\frac{\Delta\beta}{\beta}-\Delta\gamma\right)+2\frac{\Delta\rho}{\rho}+\frac{1}{2}\left(\frac{\alpha}{\beta}\right)^2(\Delta\varepsilon^v-\Delta\delta^v)\right]\sin^2\theta. \quad (1)$$

R_1 is the reflection coefficient of the S_1-wave (polarized in the isotropy plane), and R_2 is the coefficient of the S_2-wave (polarized in the symmetry plane); the superscripts *str* and *sym* denote, respectively, source–receiver azimuths along the fracture strike and in the symmetry plane; and α and β are, respectively, the P-wave and fast shear vertical velocities.

The P-wave small-angle reflection coefficient in HTI media is (Rueger, 1996)

$$R_P(\theta) = \frac{1}{2}\frac{\Delta I_P}{I_P}+\frac{1}{2}\left[\frac{\Delta\alpha}{\alpha}-\left(\frac{2\beta}{\alpha}\right)^2\left(2\frac{\Delta\beta}{\beta}+\frac{\Delta\rho}{\rho}\right)+\left(\Delta\delta^v+8\left(\frac{\beta}{\alpha}\right)^2\Delta\gamma\right)\cos^2\phi\right]\sin^2\theta, \quad (2)$$

where θ is the incident phase angle, ϕ is the angle between the source–receiver azimuth and symmetry axis, and I_p is the isotropic P-wave acoustic impedance. Inspection of equation (2) reveals that the fracture-related term $\Delta\gamma$ cannot be separated from the Thomsen-style parameter $\Delta\delta^v$ based on azimuthal variations in the P-wave AVO gradient. An explicit inversion of the P-wave AVO data gives only the quantity $\Delta\delta^v+8(\beta/\alpha)^2\Delta\gamma$. This limitation does not apply to the shear-wave data, from which $\Delta\gamma$ can be unambiguously resolved [if the porefill of the cracks is known, the change in splitting parameter can be related to the P-wave AVO gradient if the V_p/V_s ratio is known (Bakulin et al., 2000)]. The parameters δ^v and γ are important for characterizing fractures and their contents because γ is related to fracture density by the equation

$$\gamma = \frac{8}{3}\left(\frac{1-\nu}{2-\nu}\right)\eta_c \approx \eta_c \quad (3)$$

[Thomsen (1995), where η_c is the fracture density and ν is the Poisson's ratio of the unfractured medium], while δ^v is a function of both crack density and the fluid content of the cracks (wet or gas filled). While equations (1) and (3) can be used to estimate the fracture density, they do not give any information about the width, or aspect ratio, of the cracks.

The aforementioned reflection coefficient equations can be inverted at each seismic sample for each of the parameters $\Delta\rho/\rho$, $\Delta\beta/\beta$, and $\Delta\gamma$ after calculation of each AVO intercept and gradient ($\Delta\gamma$ can be found from shear-wave reflection data by subtraction of the normal-incidence shear-wave reflection coefficients). Rather than relying on simple subtraction, however, it is advantageous to adopt a weighted least-squares technique to invert the shear-wave AVO equations for the shear-wave velocity and density contrasts and $\Delta\gamma$. Weighted least squares is a generalization of the conventional least-squares regression for the case in which the relative magnitude of errors in input data can be estimated. In the intercept-gradient computation performed in AVO inversion, estimates of the resulting slope and gradients' variances are straightforward. These variances can then be used to weight the final solution, allowing a more complete use of the information contained in the seismic data. The weighted least-squares technique was chosen over generalized least squares because of the former's simplicity and practical difficulties inherent in estimating intermode covariances in the latter. The solution of the shear-wave reflection coefficient for the weighted least-squares estimate of the shear-wave splitting parameter $\Delta\gamma$ is given in the Appendix.

For the most realistic case in which the gradient variances (squared standard deviation) are substantially larger than the corresponding intercept variances, the resulting splitting parameter variance is much smaller than the variance of the fast shear-wave velocity or density. The implication that the splitting parameter is better resolved than either velocity or density is a consequence of the fact that it can be directly obtained from the intercept terms, which are inherently less noisy than the gradients.

Weighted least-squares procedures can also be applied to the estimation of the quantity $\Delta\delta^v+8(\beta/\alpha)^2\Delta\gamma$ in the P-wave seismic data by azimuth-sectoring it into a number (typically 4 to 8) of azimuth bins, computing an AVO gradient for each bin, and forming the weighted least-squares solution using the inverse variance of each bin's gradient.

DATA PROCESSING FOR MULTICOMPONENT AVO ANALYSIS

Both the P-wave and shear-wave data sets at Vacuum field were processed for interpretation of fracture density and the other contrast parameters. The converted-wave data set was not used because of the complexity of the reflection coefficient expressions for converted waves (see Rueger, 1996) and its higher noise level. The shear-wave data sets were rotated into a principal axis frame of 119° azimuth from north [derived from Alford rotation and vertical seismic profile (VSP) analysis] and were preprocessed conventionally, with amplitude recovery, Q-compensation, surface-consistent deconvolution, phase matching, residual statics and velocity analysis, and trace editing (Roche, 1997). Several iterations of statics and velocity analysis were required to achieve a reasonable statics solution.

For the shear-wave data sets, AVO-specific processing included the additional steps of azimuth-sectoring, macrobinning, and noise attenuation. Because the shear-wave reflectivity equations (1) are derived for the symmetry and isotropy planes, the shear-wave data were gathered into two azimuth slices: the first including azimuths within 30° of the symmetry

plane and the second including azimuths within 30° of the isotropy plane. Macrobinning into 5 × 5 bins (resulting in a new bin size of 275 ft, or 84 m) and offset binning in 250-ft (76-m) intervals followed to provide the trace multiplicity vital for enhancement of the data's S/N ratio. Average trace multiplicities for each offset and azimuth bin increased from 20–25 in the near-offset range to 40–50 in the medium offsets. The maximum usable offset in the shear-wave data was approximately 3000 ft (914 m).

Because of the presence of a substantial amount of noise in the data, additional enhancement was performed using f-x deconvolution and a mild five-trace 3-D trace mix in the common-offset domain. Both of these processes, while smearing the data somewhat, resulted in a substantial improvement in data quality and were made more effective by the extremely slight dips present in the San Andres and overburden at Vacuum field. A final time alignment of the slow and fast modes at the reservoir level was required to prepare the data for AVO analysis.

Weighted least-squares AVO analysis using weighted stacks followed AVO preprocessing. Generation of these stacks for the change in splitting parameter, fast shear-wave velocity, and density involved (1) estimating the AVO intercept and gradient at each time sample for each input mode, (2) computing the variances for each of these quantities at each time sample, (3) forming the weights by computing the inverse of the variances, and (4) combining the AVO intercepts, gradients, and weights using equations (7)–(10) to obtain estimates of the change in the splitting parameter and its variance. Weighted stacks, while sensitive to residual moveout, are much simpler to generate and interpret than methods requiring event-tracking techniques in the prestack domain. Stacks of standard deviation for each attribute were also generated to allow an assessment of the quality of each measurement.

Raw intercept and gradient stacks for the S_1^{sym} and S_2^{str} modes are shown (separately gained) in Figure 4. Examination of the computed weights revealed that the intercept weights were generally considerably greater than the gradient weights, as expected; still, the shear-wave gradient weights made a considerable contribution (Figure 5). A stack along in-line 71 of the change in splitting parameter and its standard deviation are shown in Figure 6. The section above 1 s is seen to have a high-amplitude response indicative of fracturing but also a large standard deviation because of its strong reflectivity and consequently greater scatter. The splitting parameter stack made from the time-aligned S_1^{sym} and S_2^{str} modes had the highest data quality.

A similar processing flow (without vector rotation) was applied to the P-wave data (Roche, 1997), including AVO preprocessing steps such as 5 × 5 macrobinning and random noise attenuation. Because equation (2), the P-wave linearized reflection coefficient, is valid for arbitrary azimuths, analysis is not restricted to the medium's symmetry planes, and a total of six 15° azimuth slices was used. Figure 7 shows four of the six azimuth slices for the 2000-ft (610-m) offset for a representative in-line. Unfortunately, considerable variability attributable to noise is seen at the objective level (at 600–650 ms two-way time).

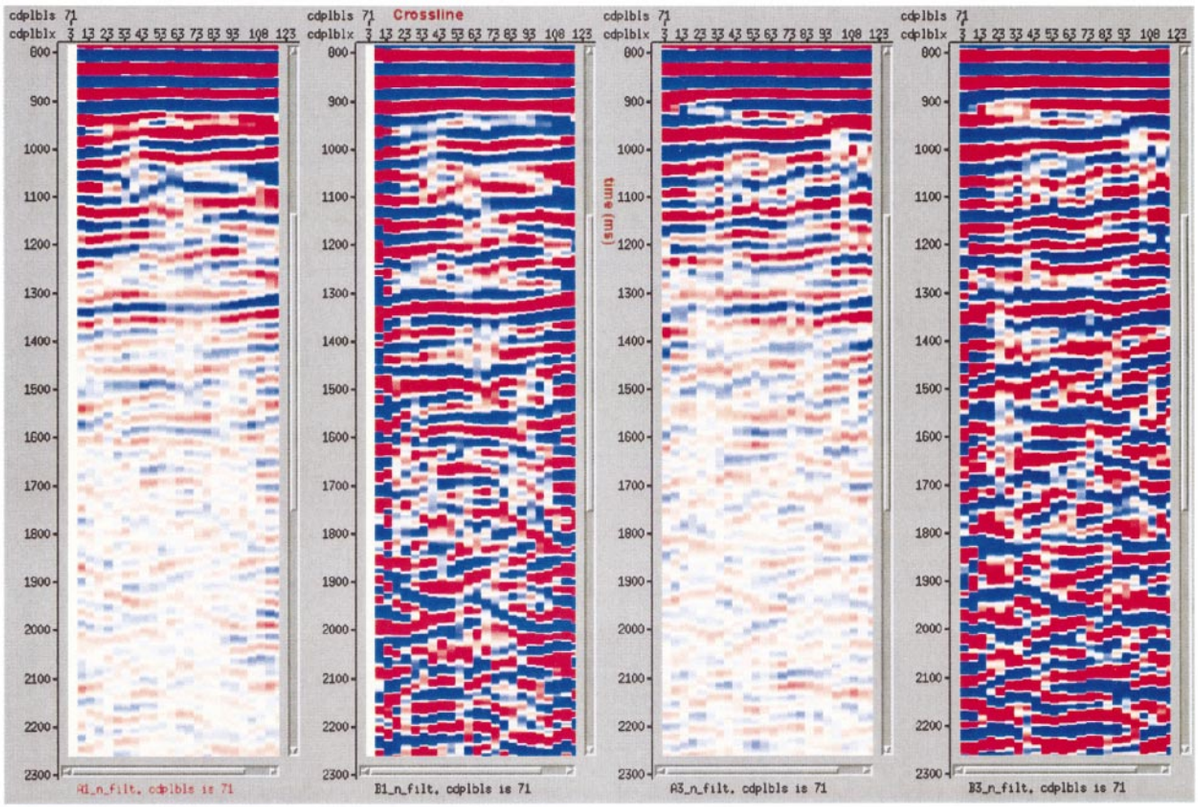

FIG. 4. Shear-wave AVO intercepts (left and center-right) and gradients (center-left and right), in-line 71. Red is negative amplitudes; blue, positive. The San Andres reservoir interval is at approximately 1600 ms.

Weighted least-squares stacks of the azimuthal variation in AVO gradient were then computed. As is evident from equation (2), the azimuthal variation in AVO gradient is controlled by the term $\Delta\delta^v + 8(\beta/\alpha)^2\Delta\gamma$. Because this fracture-related term appears only in the AVO gradient, its response was considerably noisier than that of its shear-wave counterpart, in which the splitting parameter is present in the AVO intercepts. The large amount of noise-related variability in the P-wave azimuth slices is reflected in the large standard deviations seen in the azimuthal gradient stacks (Figure 8). Standard deviations were generally observed to be greater for the P-wave data than for the shear-wave results, as discussed below.

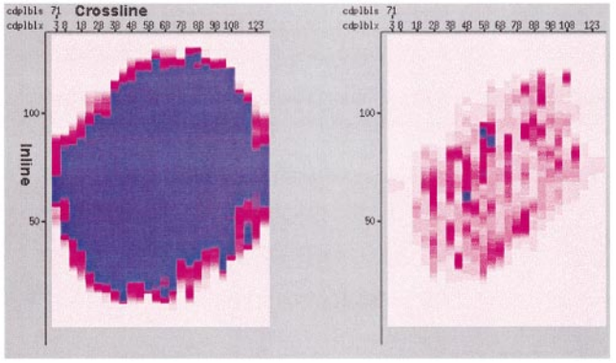

FIG. 5. Intercept (left) and gradient (right) weights, S_2^{str} mode, time slice at 1688 ms (within the San Andres reservoir interval). Darker colors indicate larger relative values of weight.

AVO INTERPRETATION

The most useful data set for studying fracturing at the primary reservoir level proved to be the splitting parameter $\Delta\gamma$ stack volume obtained using the S_1^{sym} and S_2^{str} volumes. Additionally, the fractional change in fast shear-wave velocity $\Delta\beta/\beta$ was used to make inferences about fracturing in directions other than the fast shear-wave polarization direction, because low-aspect pores or fractures having orientations other than the S_1 direction may reduce the fast shear-wave velocity of the rock.

The most prominent event on the splitting parameter stack in the Upper and Middle San Andres interval is a peak at approximately 1650 ms two-way shear time which is continuous and readily interpretable across the survey area. A relative amplitude map of this event [overlain by faults interpreted at the reservoir level by Talley (1997)] is shown in Figure 9. High values of this relative amplitude correspond to higher values of $\Delta\gamma$, indicating large values of γ for the San Andres, because the overlying Grayburg and uppermost San Andres are relatively unfractured (Scuta, 1997). Examination of Figure 9 reveals that areas of anomalously high fracture density occur in the vicinity of fault bends, particularly in the northwestern portion of the survey area (at a prominent fault bend near cross-line 100) and to the south of the injector well CVU-97. Both numerical models and field studies predict fracturing in the vicinity of fault bends because of stress concentration, particularly if the fault has a component of oblique-slip motion (Du and Aydin, 1995; Segall and Pollard, 1980). Interestingly, the time-lapse shear-wave splitting anomaly associated with carbon dioxide injection in well CVU-97 (Talley, 1997) occurs in an area interpreted to have anomalously high fracture intensity south of that well.

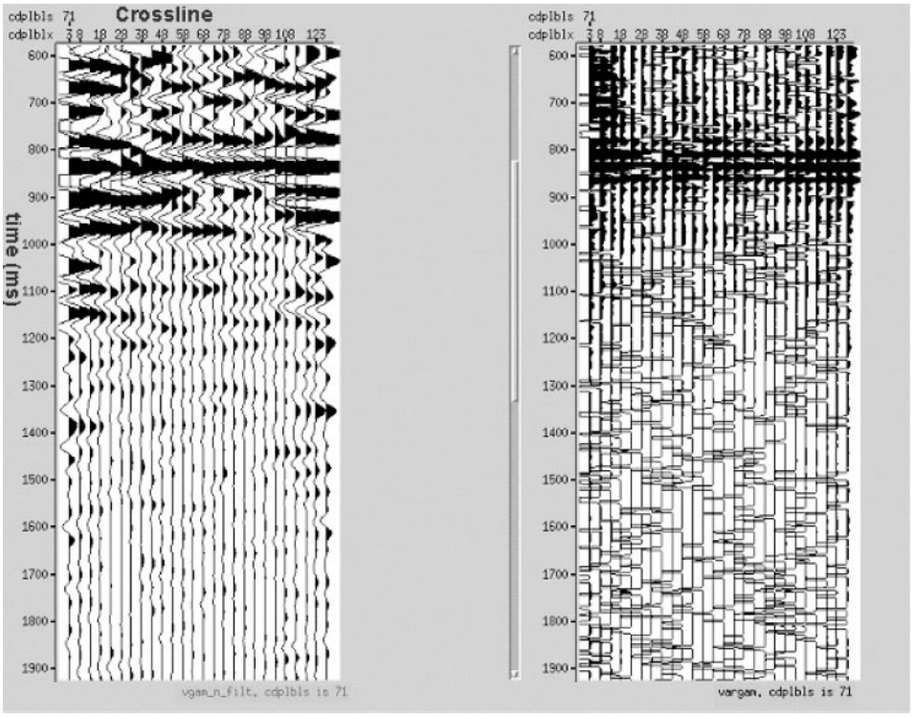

FIG. 6. Splitting parameter ($\Delta\gamma$) stack (left) from shear-wave data made using weighted least-squares AVO analysis and commonly gained standard deviations (right), in-line 71.

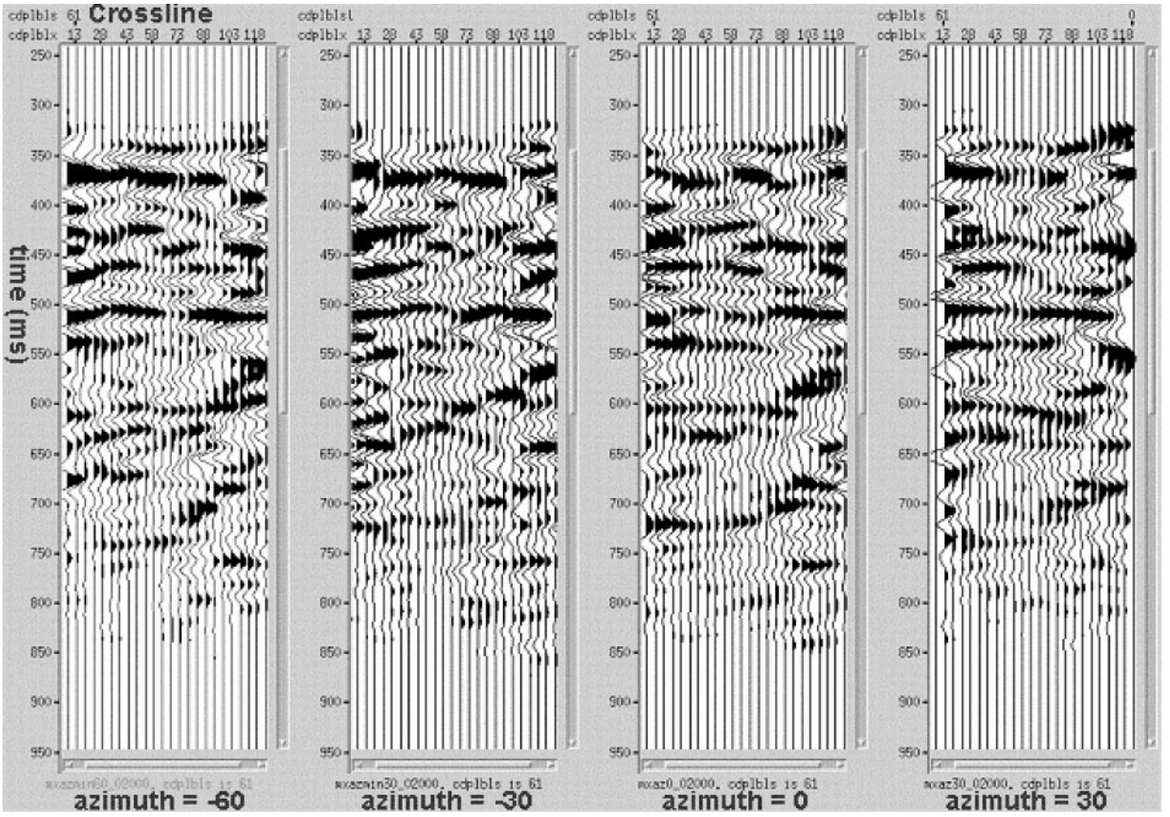

FIG. 7. *P*-wave azimuth slices, in-line 61, for 2000-ft offset. Note variability present in areas of weaker reflectivity, particularly at the San Andres reservoir level (550–600 ms).

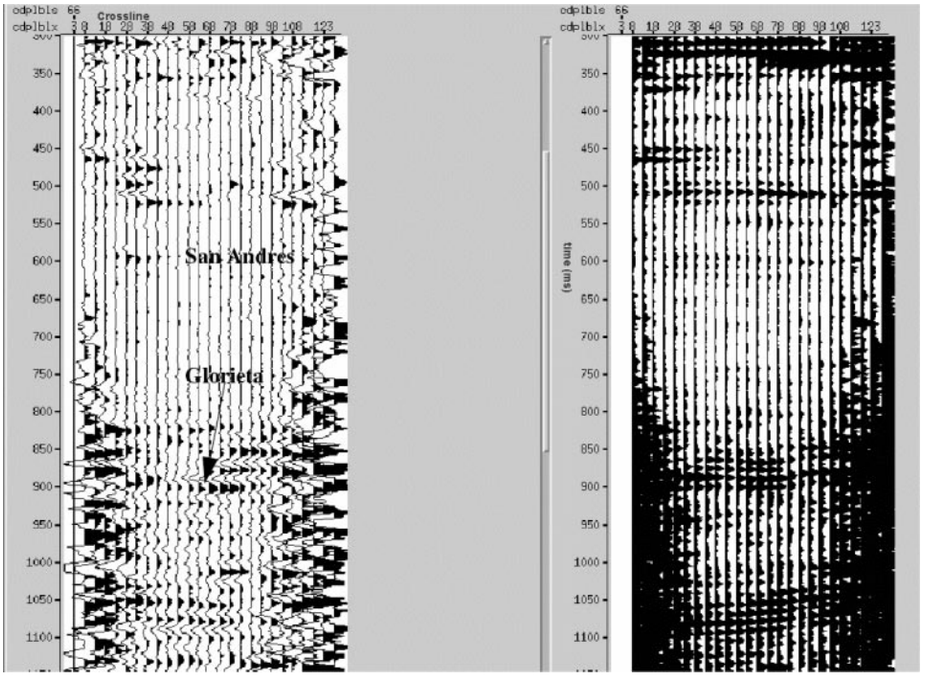

FIG. 8. *P*-wave azimuthal gradient stack (left) with commonly gained standard deviation estimate (right), in-line 66. Note weak reservoir reflectivity and relatively large standard deviations.

The San Andres splitting parameter ($\Delta\gamma$) amplitude shown in Figure 9 is an excellent predictor of well fluid productivity at reservoir level, as indicated in Figure 10, for which San Andres fluid production is crossplotted against splitting parameter amplitude. Very good agreement ($R^2 = 0.87$) is observed between well fluid productivity and wells in the northern half of the study area, as indicated by the topmost regression line in Figure 10. A second productivity trend for wells south of well CVU-97 is also observed ($R^2 = 0.68$). The presence of two spatially separated permeability regimes in the San Andres over the study area is a result of more compartmentalization both from small-scale faulting near the shelf edge and from a greater degree of anhydrite cementation in the San Andres in the southern portion of the survey area (Scuta, 1997).

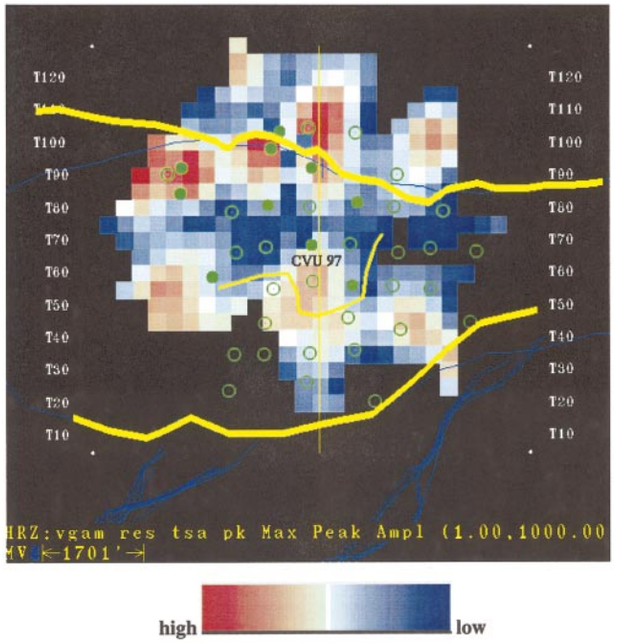

FIG. 9. Upper San Andres splitting parameter ($\Delta\gamma$) amplitude map of study area, picked from splitting parameter stack volume, with higher relative values of fracture intensity shown in red. Interpreted San Andres faults are shown in yellow.

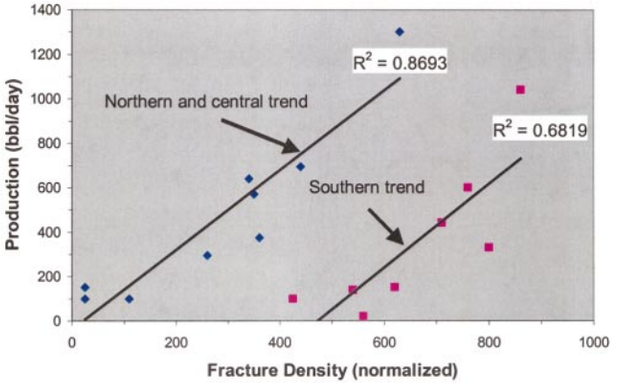

FIG. 10. Crossplot of $\Delta\gamma$ stack horizon shown in Figure 9 against San Andres fluid production (vertical axis) in barrels/day.

Fair agreement is observed between time-interval shear-wave splitting measurements from the S_1 and S_2 stacked sections over a much larger vertical interval (the Queen to Lower San Andres) and the splitting parameter amplitude shown in Figure 9. Figure 11 shows the splitting parameter amplitude overlain (in colored contour lines) on a map of time-interval splitting measured between the Queen and Lower San Andres, an interval approximately 700 ft (213 m) thick. While good agreement is observed in the northwestern, southeastern, and southwestern portions of the survey area, the area of the time-lapse anomaly (Talley, 1997) is seen to have much less AVO-derived splitting (on the initial survey) than indicated by the time-interval measurements. Perfect correlation between interval-derived splitting measurements and AVO results should not be expected in any event given their different vertical resolution [700 ft (213 m) for the interval measurement versus 100–200 ft (30–60 m) for amplitude-based results].

The use of weighted least-squares techniques also allows formal error estimates of each AVO attribute to be computed. A map of the percentage of standard deviations for the splitting parameter stack amplitude horizon of Figure 9 is shown in Figure 12. It is apparent that most standard deviations cluster in the 20–50% range in fractured regions (with a relatively constant overall absolute level), indicating a relatively reliable result compared to other techniques. As discussed below, the shear-wave standard deviations proved considerably lower than their P-wave azimuthal AVO counterparts. Standard deviations in the northern, more productive part of the

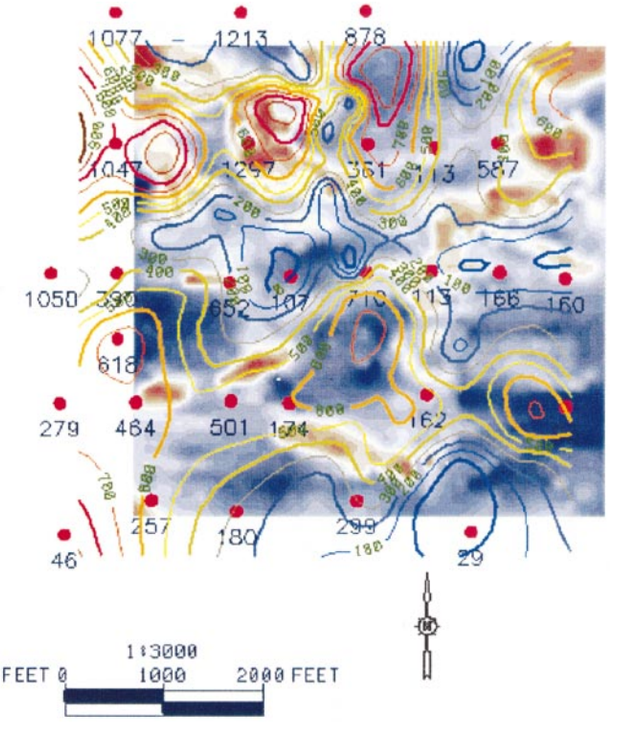

FIG. 11. Queen to Lower San Andres shear-wave splitting map [from Talley (1997) with red values indicating a large amount of splitting; blue, relatively little splitting] overlain by colored line contours of the splitting parameter stack of Figure 9, with wells displayed in red.

study area tend to be slightly less than those observed in the southern portion of the field, where the presence of anhydrite leads to a lower level of fluid production for a given porosity or fracture intensity.

An added benefit of multicomponent AVO analysis is that the change in fast shear-wave velocity can be used to map the presence of fractures open in subsidiary, or even random, directions. A map of the fast (S_1) shear-wave velocity contrast parameter generated from stack volumes of the shear-wave gradient and splitting for the Upper San Andres is shown in Figure 13. While the noise associated with the shear-wave velocity contrast parameter is much greater than that for the splitting parameter, an intriguing area of decreasing shear-wave velocity is seen in the area of the time-lapse anomaly to the south of injector well CVU-97. One possible explanation for this is an increased concentration of open fractures or low-aspect porosity (crack-like pores having a high length-to-width ratio) oriented at an angle to the fast direction; such inclusions may influence the S_1 velocity (while also giving rise to lower-order anisotropic symmetries). Indeed, striking agreement is observed between the Upper/Middle San Andres $\Delta\beta/\beta$ values and the corresponding V_p/V_{S_1} measurements (DeVault, 1997).

The shear-wave results described above were compared with interpretations of fracturing using azimuthal P-wave AVO analysis only to estimate the parameter $\Delta\delta^v + 8(\beta/\alpha)^2\Delta\gamma$ [which can be shown to approximately equal $\Delta\gamma$ for fluid-filled inclusions (Rueger, 1996)]. Unfortunately, performance of the P-wave-only azimuthal AVO analysis generally proved somewhat inferior to shear-wave methods over the San Andres reservoir in the study area. Azimuthal AVO gradient at the Upper San Andres computed using weighted least squares and overlain by percentage error contours is shown in Figure 14. This AVO attribute proved to be less well correlated with well fluid production than its shear-wave counterpart, although some correlation does indeed exist (DeVault, 1997). Additionally, as seen from Figure 14, standard deviations for this attribute are uniformly greater than 100%, indicating a low level of reliability.

DISCUSSION AND CONCLUSIONS

The use of weighted least-squares techniques for analyzing seismic amplitudes in the prestack domain allows explicit estimation of noise level in AVO attributes and assessment of the reliability of interpretation results. Processes such as AVO, which involve statistical fitting procedures (computation of slopes and intercepts), are ideally suited for weighted least-squares techniques, since the fit quality estimated during the intermediate steps can be used as weights in subsequent calculations. The linearized shear-wave reflection coefficients in the symmetry planes of HTI media can be inverted using weighted least-squares formalism for the contrast in fast shear-wave velocity, density, and the splitting parameter γ. For HTI media with a single system of penny-shaped inclusions, γ is close to the density of fractures or fracture-like inclusions present (Thomsen, 1995).

Interpretation of shear-wave AVO attributes reveals that the San Andres reservoir section in the study area at Vacuum field is fractured and that its production characteristics (e.g.,

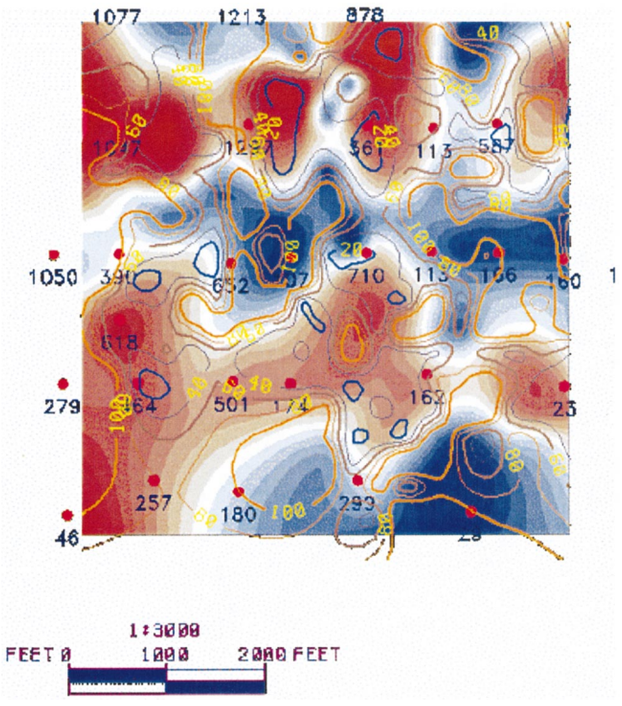

FIG. 12. San Andres fracture amplitude map of Figure 9 overlain by percentage standard deviation contours, contoured with a 20% increment.

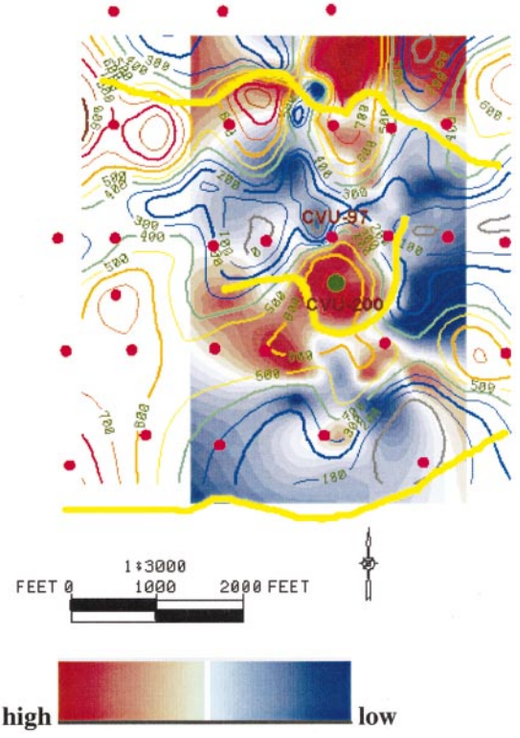

FIG. 13. Upper San Andres shear-velocity fractional difference ($\Delta\beta/\beta$) horizon map (with red indicating high values; blue, low values) with splitting parameter ($\Delta\gamma$) stack amplitude of Figure 9 overlain as line contours. Major San Andres-level faults are shown in yellow. Note area of high amplitude south of well CVU-97.

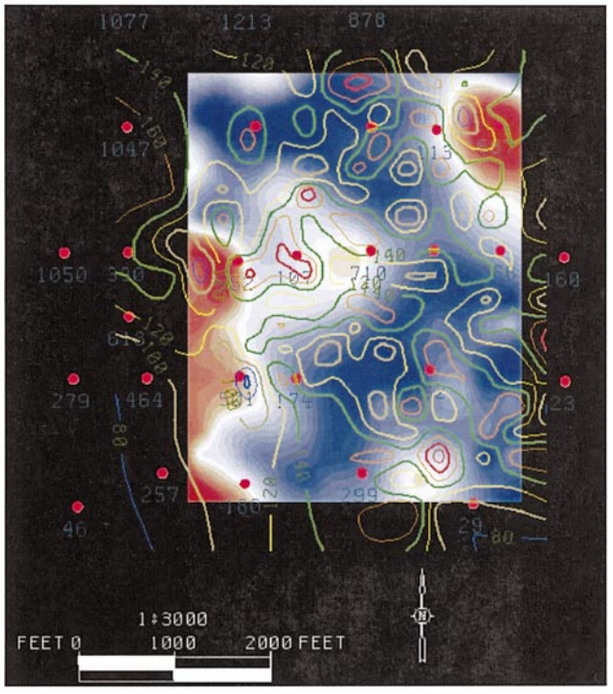

FIG. 14. Variation in P-wave azimuthal AVO gradient for the Upper San Andres, overlain by contoured percentage standard deviations. Well daily fluid production (in barrels/day) is posted below well locations. Compare with corresponding shear-wave result in Figure 12.

reservoir-scale permeability) are strongly influenced by fractures. These conclusions were drawn as the direct result of applying geophysical techniques to reservoir characterization. Striking correlation between γ obtained from the shear-wave AVO data and field production behavior is observed. Fracturing has also been observed at other San Andres reservoirs in the Permian Basin, such as Keystone field on the Central Basin Platform (Major and Holtz, 1997).

The location of areas of increased fracturing in the Vacuum field study area can be explained geologically by proximity to bends in faults having an oblique-slip component of displacement. Fracturing also appears more prevalent in areas near the shelf edge in the southernmost portion of the survey area. The presence of a fast shear-wave velocity anomaly in the area of the time-lapse anomaly may suggest a second set of open fractures to the south of the carbon dioxide injection well.

The relatively poor performance of P-wave azimuthal AVO compared to shear-wave AVO is a result of the weaker sensitivity of P-wave reflectivity to fracturing. The splitting parameter contrast $\Delta\gamma$ appears only in the gradient term of the P-wave reflection coefficient, while for S-waves it appears in the much more robustly estimated intercepts of the reflection coefficients [equation (1)]. P-wave azimuthal AVO analysis has been shown to succeed in more heavily fractured settings or with higher-quality input data (e.g., Lynn et al., 1996). In any event, as with shear-wave AVO analysis, adapting the weighted least-squares formalism to azimuthal P-wave AVO also allows more reliable estimates of attribute noise levels than those obtained by comparison of AVO gradients from various azimuths alone. If a lower level of vertical resolution is acceptable, as may be the case for thick fractured intervals, use of P-wave moveout data may also provide useful quantitative estimation of fracture density through inversion of the NMO ellipse.

ACKNOWLEDGMENTS

The authors thank the members and industry sponsors of the Reservoir Characterization Project for their support. Particular thanks are offered to Steve Roche, Danny Talley, and Bruce Mattocks for many useful discussions. The authors also thank the staff of Geophysical Development Corporation, particularly Connie Van Schuyver for valuable assistance in software development and data processing and Jay Blaylock for several figures.

REFERENCES

Bakulin, A., Grechka, V., and Tsvankin, I., 2000, Estimation of fracture parameters from reflection seismic data—Part I: HTI model due to a single fracture set: Geophysics, **65**, 1788–1802.

Bebout, D. G., and Harris, P. M., 1990, Geologic and engineering approaches in evaluation of San Andres/Grayburg hydrocarbon reservoirs, Permian basin: Bureau of Econ. Geol., Univ. of Texas at Austin.

Blaylock, J., 1999, Interpretation of a baseline 4-D multicomponent seismic survey at Vacuum field, Lea County, New Mexico: M.S. thesis, Colorado School of Mines.

DeVault, B. C., 1997, Prestack multicomponent amplitude analysis, Vacuum Field, Lea County, New Mexico: Ph.D. thesis, Colorado School of Mines.

Du, Y., and Aydin, A., 1995, Shear fracture patterns and connectivity at geometric complexities along strike-slip faults: J. Geophys. Res., B9, **100**, 18093–18102.

Lynn, H. B., Simon, K. M., Bates, C. R., and Van Dok, R. R., 1996, Azimuthal anisotropy in P-wave 3-D (multiazimuth) data: The Leading Edge, **15**, No. 8, 931–936.

Major, R. P., and Holtz, M. H., 1997, Identifying fracture orientation in a mature carbonate platform reservoir: AAPG Bulletin, **81**, 1063–1069.

Mattocks, B., 1997, Borehole geophysical investigation of seismic anisotropy at Vacuum Field, Lea County, New Mexico: Ph.D. thesis, Colorado School of Mines.

Roche, S. L., 1997, Time-lapse, multicomponent, three-dimensional seismic characterization of a San Andres shallow shelf carbonate reservoir, Vacuum field, Lea County, New Mexico: Ph.D. thesis, Colorado School of Mines.

Roche, S. L., Davis, T. L., and Benson, R. D., 1997, 4-D, 3-C seismic study at Vacuum field, New Mexico: 67th Ann. Internat. Mtg., Soc. Expl. Geophys., Expanded Abstracts, 886–889.

Rueger, A., 1996, Analytic insight into shear-wave AVO for fractured reservoirs: 66th Ann. Internat. Mtg., Soc. Expl. Geophys., Expanded Abstracts, 1801–1804.

——— 1998, Variation of P-wave reflectivity with offset and azimuth in anisotropic media: Geophysics, **63**, 935–947.

Scuta, M., 1997, 3-D geological characterization of the central Vacuum unit, Lea County, New Mexico: Ph.D. thesis, Colorado School of Mines.

Seber, 1977, Linear regression analysis: John Wiley & Sons, Inc.

Segall, P., and Pollard, D., Mechanics of discontinuous faults: J. Geophys. Res., B8, **85**, 4337–4350.

Talley, D. J., 1997, Characterization of a San Andres carbonate reservoir using four-dimensional, multicomponent attribute analysis: M.S. thesis, Colorado School of Mines.

Thomsen, L., 1995, Elastic anisotropy due to aligned cracks in porous rock: Geophys. Prosp., **43**, 805–829.

Tsvankin, I., 1995, Body-wave radiation patterns and AVO in transversely isotropic media: Geophysics, **60**, 1409–1425.

——— 1997, Reflection moveout and parameter estimation for horizontal transverse isotropy: Geophysics, **62**, 614–629.

Voorhies, C. H., 1996, Application of a multicomponent vertical seismic profile to dynamic reservoir characterization at Vacuum field, Lea County, New Mexico: M.S. thesis, Colorado School of Mines.

APPENDIX

DERIVATION OF WEIGHTED LEAST-SQUARES SHEAR-WAVE REFLECTION COEFFICIENTS

The general weighted least-squares problem may be expressed in matrix form (Seber, 1977) as

$$\mathbf{y} = \mathbf{X}\mathbf{b} + \mathbf{e}, \tag{A-1}$$

where $\mathbf{y}$ is the measured system response, $\mathbf{b}$ is the solution vector, $\mathbf{X}$ is the regressor matrix, and $\mathbf{e}$ is the noise vector. Weighted least-squares methodologies make the additional assumption that the noise vector $\mathbf{e}$ takes the form $\sigma^2\mathbf{V}$, where $\mathbf{V}$ is a known, diagonal matrix. Minimizing the squared norm of the vector $\mathbf{y} - \mathbf{X}\mathbf{b}$ gives the least-squares estimate (Seber, 1977) for $\mathbf{b}$,

$$\mathbf{b}^* = (\mathbf{X}^{\mathrm{T}}\mathbf{V}^{-1}\mathbf{X})^{-1}\mathbf{X}^{\mathrm{T}}\mathbf{V}^{-1}\mathbf{y}. \tag{A-2}$$

Applying this formalism to the HTI shear-wave reflection coefficient equation (1) [omitting the AVO gradients for the R_2^{sym} and R_1^{str} modes, which were contaminated by radiation-pattern related energy focusing resulting from the slight vertical transverse isotropy observed in the subsurface at Vacuum Field; see Tsvankin (1995) and Mattocks (1997)], the following linear system is obtained:

$$\begin{bmatrix} A_1 \\ B_1 \\ A_2 \\ A_3 \\ B_3 \\ A_4 \end{bmatrix} = \begin{bmatrix} -\frac{1}{2} & -\frac{1}{2} & 0 \\ \frac{1}{2} & 0 & -\frac{1}{2} \\ -\frac{1}{2} & -\frac{1}{2} & \frac{1}{2} \\ -\frac{1}{2} & -\frac{1}{2} & \frac{1}{2} \\ \frac{1}{2} & 0 & -\frac{1}{2} \\ -\frac{1}{2} & -\frac{1}{2} & 0 \end{bmatrix} \begin{bmatrix} \frac{\Delta\beta}{\beta} \\ \frac{\Delta\rho}{\rho} \\ \Delta\gamma \end{bmatrix}, \tag{A-3}$$

where the linearized equations are parameterized in the form $R = A + B\sin^2\theta$; the normal-incidence term AS_1^{sym} is written as A_1; AS_2^{sym} becomes A_2; AS_2^{str} becomes A_3; and AS_1^{str} becomes A_4. The same convention is adopted for each of the retained AVO gradients B. Solving this system analytically gives a weighted least-squares expression for the contrast in splitting parameter γ,

$$\Delta\gamma = \frac{E}{F}, \tag{A-4}$$

where

$$E = 2\begin{bmatrix} -w_1w_2w_3(A_1 - A_2) + w_2w_1w_4(A_1 + A_3) \\ + w_1w_3w_5(A_2 - A_1) + w_1w_4w_5(A_3 - A_1) \\ + w_2w_3w_6(A_2 - A_4) + w_2w_4w_6(A_3 - A_4) \\ + w_3w_5w_6(A_2 - A_4) + w_4w_5w_6(A_3 - A_4) \end{bmatrix} \tag{A-5}$$

and

$$F = w_1w_2w_3 + w_1w_2w_4 + w_1w_3w_5 + w_1w_4w_5 + w_2w_3w_6 + w_2w_4w_6 + w_3w_5w_6 + w_4w_5w_6. \tag{A-6}$$

The weights w_i are the inverse variances in the shear-wave AVO intercepts and gradients numbered in the order of the rows of the left-hand side of equation (A-3). The variance in the splitting parameter γ is

$$\sigma_\gamma^2 = 4\left[\frac{w_1w_2 + w_2w_3 + w_2w_4 + w_1w_5 + w_3w_5 + w_4w_5 + w_2w_6 + w_5w_6}{F}\right], \tag{A-7}$$

where F is given in equation (A-6).